Multiple Metal Binding Domains Enhance the Zn(II) Selectivity of the Divalent Metal Ion Transporter AztA†

Tong Liu,‡ Hermes Reyes-Caballero,‡ Chenxi Li,§ Robert A. Scott,§ and David P. Giedroc*,‡

Department of Biochemistry and Biophysics, Texas A&M University, College Station, Texas 77843-2128, and Department of Chemistry and Center for Metalloenzyme Studies, University of Georgia, Athens, Georgia 30602

Received April 3, 2007; Revised Manuscript Received July 17, 2007

ABSTRACT: Transition metal-transporting P_{1B}-type CPx ATPases play crucial roles in mediating metal homeostasis and resistance in all cells. The degree to which N-terminal metal binding domains (MBDs) confer metal specificity to the transporter is unclear. We show that the two MBDs of the Zn/Cd/Pb effluxing pump *Anabaena* AztA are functionally nonequivalent, but only with respect to zinc resistance. Inactivation of the a-MBD largely abrogates resistance to high intracellular Zn(II) levels, whereas inactivation of the b-MBD is not as deleterious. In contrast, inactivation of either the a- or b-MBD has little measurable impact on Cd(II) and Pb(II) resistance. The membrane proximal b-MBD binds Zn(II) with a higher affinity than the distal N-terminal a-MBD. Facile Zn(II)-specific intermolecular transfer from the a-MBD to the higher-affinity b-MBD is readily observed by $^1H-^{15}N$ HSQC spectroscopy. Unlike Zn(II), Cd(II) and Pb(II) form saturated 1:1 S_4 or S_3(O/N) complexes with $AztA^{aHbH}$, where a single metal ion bridges the two MBDs. We propose that the tandem MBDs enhance Zn(II)-specific transport, while stabilizing a non-native inter-MBD Cd/Pb cross-linked structure that is a poor substrate and/or regulator for the transporter.

Complex metal homeostasis and trafficking systems control the bioavailability of essential transition metal ions while ensuring that these and other abiological xenobiotics, including Cd, Pb, Hg, and As, do not accumulate inside cells. The heavy metal ion-transporting CPx-ATPases represent a large subfamily of P-type ATPases (P_{1B}-type) found in both prokaryotes and eukaryotes that play important roles in metal homeostasis (*1*−*5*). All are characterized by eight transmembrane (TM)[1] helices that likely form the channel for transport. TM6 bears the CPx signature sequence, which is thought, in conjunction with other residues in the membrane helices, to coordinate the metal during transport (*6*). Large cytoplasmic loops are folded into structurally characterized actuator (*7*) [A-domain (Figure 1A)] and ATP binding domains (*8*, *9*) (N- and P-domains), with metal translocation coupled to phosphorylation of an aspartate residue in the P-domain.

Another significant feature of CPx-ATPases is that most have N-terminal and/or C-terminal cytosolic extensions, often containing one or more tandemly linked ferredoxin fold-like $\beta\alpha\beta\beta\alpha\beta$ metal binding domains (MBDs) (Figure 1A) (*10*). For example, the Wilson's and Menkes disease Cu/Ag-specific ATPases ATP7A and ATP7B, respectively, have six tandemly linked MBDs, while those from lower eukaryotes and most prokaryotes have zero, one, or two MBDs. These MBDs are known to provide docking sites for Cu chaperones that allow Cu to be handed off, via intermolecular metal−ligand exchange reactions, to partner MBDs without dissociation of the metal into bulk solution (*11*−*14*). This provides strong support for the central tenet of the Cu-trafficking hypothesis (*15*, *16*). Mechanistic studies with *Archaeglobus fulgidis* CopA suggest that metal binding to the single N-terminal MBD plays a regulatory role in enhancing the rate of dephosphorylation of the phosphoaspartate residue in the E2 state; this increases the rate of metal ion release which is rate-limiting in multiple-turnover experiments (*17*).

Some divalent metal ion (Zn/Cd/Pb)-specific P_{1B}-type ATPases (*2*) are also known to possess an MBD, but the functional role that this domain plays is a topic of ongoing investigation. Since there are no known zinc chaperones, the significance of protein−protein docking and intermolecular transfer is unclear. However, there is some evidence in support of the idea that the specific structural features of individual MBDs might provide some metal selectivity to

† This work was supported by grants from the National Institutes of Health (NIH) (GM042569 to D.P.G. and GM042025 to R.A.S.) and the Robert A. Welch Foundation (A-1295 to D.P.G.). Portions of this research were carried out at the Stanford Synchrotron Radiation Laboratory (SSRL), operated by Stanford University on behalf of the U.S. Department of Energy, Office of Basic Energy Sciences. The SSRL Structural Molecular Biology Program is supported by the Department of Energy, Office of Biological and Environmental Research, and by the NIH National Center for Research Resources, Biomedical Technology Program.

* To whom correspondence should be addressed: Department of Chemistry, Indiana University, 800 E. Kirkwood Ave., Bloomington, IN 47405-7102. Telephone: (812) 856-5449. Fax: (812) 855-8300. E-mail: giedroc@indiana.edu.

‡ Texas A&M University.

§ University of Georgia.

[1] Abbreviations: ArsR, arsenic repressor; *azt*, *Anabaena* zinc transport; $AztA^{aH}$, N-terminal a-MBD with a His-rich tail (residues 1−105); Azt^{aHbH}, complete MBD of AztA (residues 1−213); mag-fura-2, 2-{6-[bis(carboxymethyl)amino]-5-(carboxymethoxy)-2-benzofuranyl}-5-oxazolecarboxylic acid; MBD, metal binding domain; TM, transmembrane.

10.1021/bi7006367 CCC: $37.00
Published on Web 09/08/2007

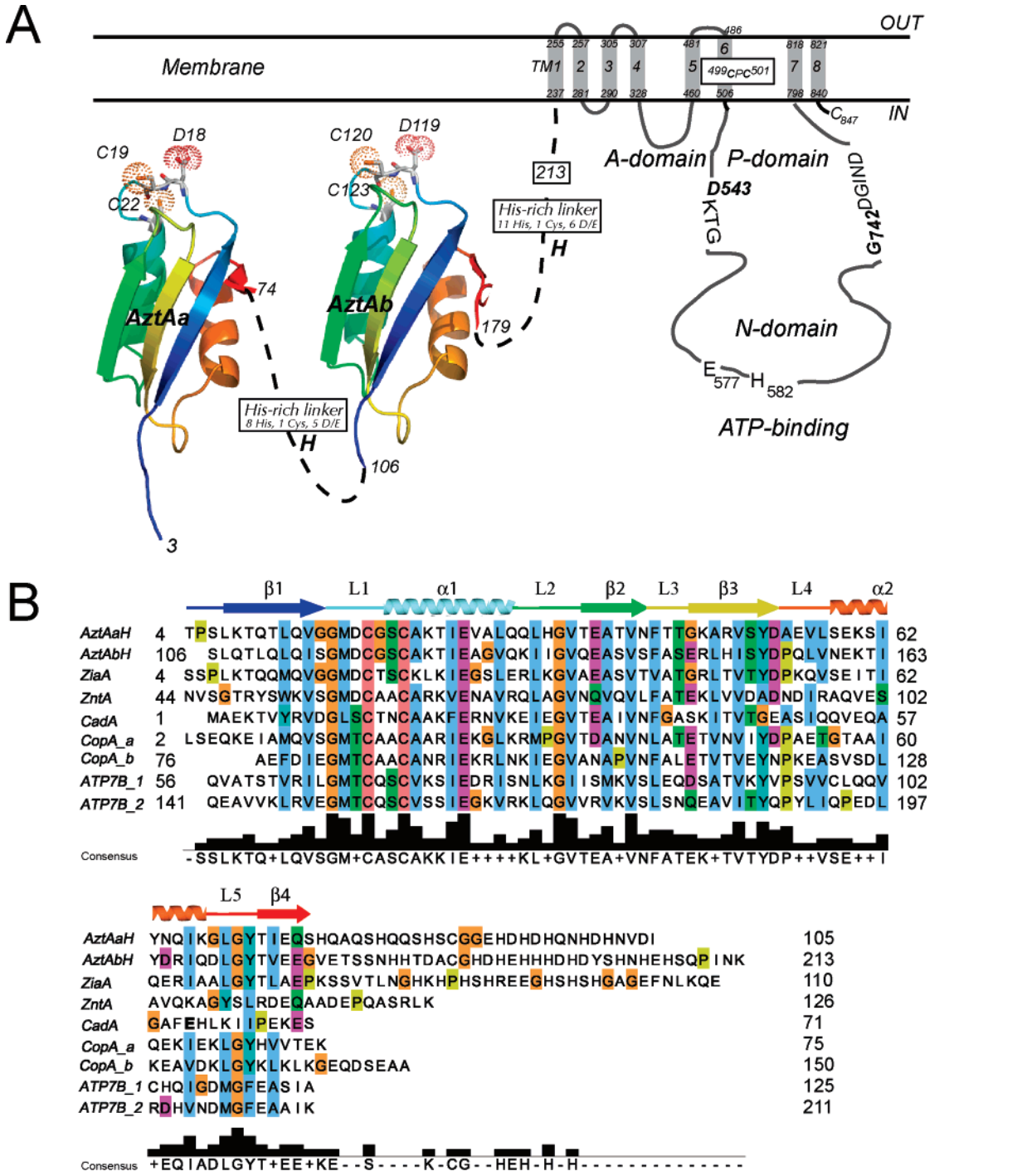

FIGURE 1: (A) Schematic representation of the domain structure of AztA showing the two tandem MBDs followed by an ≈30-residue hydrophilic His-rich linker. The predicted eight transmembrane helices, cytosolic ATP binding domains (N and P), and actuator domain (A), and putative CPC intramembrane zinc transport site are shown. The homology models of the AztA a-MBD and b-MBD were generated using *B. subtilis* CopAa (PDB entry 1OPZ) as a template using Swiss-Model (http://swissmodel.expasy.org//SWISS-MODEL.html). (B) Sequence alignment of the N-terminal region of AztA with analogous domains associated with other divalent or monovalent CPx-ATPases. The sequences are the first and second MBDs of *Anabaena* PCC 7120 AztA, ZiaA from *Synechocystis* spp. PCC 6803, ZntA from *E. coli*, CopA_a and CopA_b from *B. subtilis*, and the first and second MBDs from the Wilson disease ATPase, ATP7B. The deduced secondary structure derived for $AztA^{aH}$ is also shown.

the transporter itself, despite the fact that they all adopt essentially the same $\beta\alpha\beta\beta\alpha\beta$ fold (*10*) and all metal complexes employ the two conserved Cys residues of the CXXC sequence as metal donor atoms (*18*−*21*). For example, in both copper chaperones and MBDs derived from Cu/Ag transporters, the Cu(I) is often coordinated via a linear bis-thiolate complex (*22*−*24*); in another case, a distorted trigonal S_2N complex is found, where a His derived from loop 5 between helix α2 and strand β4 is a ligand (*25*). For the Zn/Cd/Pb transporter *Escherichia coli* ZntA, a conserved Asp just N-terminal to the first Cys (**D**CXXC) was proposed to drive 3- or 4-coordination of Zn(II) (*19*); in contrast, for the Cd/Pb-selective transporter *Listeria monocytogenes* CadA, a conserved Glu in loop 5 (E61 in Figure 1B) appears to form a coordination bond to the Cd(II) in a binuclear homodimeric subunit bridging structure (*20*).

Anabaena AztA (alr7622) is a P_{1B}-type ATPase efflux pump encoded by the *azt* (*Anabaena* zinc transport) operon whose expression is transcriptionally induced upon direct binding of Zn, Pb, or Cd by the ArsR (or ArsR/SmtB) family (*26*) regulator AztR (*27*). AztA possesses the unique functional property of conferring significant Zn(II) resistance to a transformed Zn/Cd/Pb-hypersensitive *E. coli* strain (GG48), relative to Cd(II) and Pb(II) (*27*). In fact, cadmium and lead resistance is barely detectable relative to that conferred by other known Pb/Cd/Zn-transporting ATPases, including *E. coli* ZntA (*28*) and CadAs from *Streptomyces aureus*, *Ralstonia metallodurans*, and *L. monocytogenes* (*29*). AztA is also distinguished from other characterized Zn/Cd/Pb transporters on the basis of harboring two N-terminal MBDs, each of which is followed by an ≈30-residue hydrophilic His-rich linker (Figure 1). The two MBDs of AztA are 44% identical, pairwise, in amino acid sequence (71% similar), and each contains a DCXXC sequence and lacks the Glu in loop 5 found in CadAs. Since AztA is unique in incorporating tandem MBDs followed by His-rich segments, this led us to hypothesize that some aspect of these specific features might confer higher selectivity for Zn(II) relative to Cd(II) and Pb(II).

In this report, we show that the two MBDs of *Anabaena* AztA play nonredundant structural and functional roles in metal binding and heavy metal resistance in vivo, but only with respect to zinc resistance. We show that the membrane proximal b-MBD has a higher affinity for Zn(II) than the distal a-MBD, and consistent with this, Zn(II) prebound to the a-MBD facilely moves to a metal-free b-MBD. However, the low-affinity a-MBD plays a critical role in mediating zinc resistance under conditions of high zinc toxicity in a manner that does not require the b-MBD. This suggests that the a-MBD is capable of functioning in a manner independent of the b-MBD in maximally stimulating transport under high intracellular zinc loads. In contrast, both Cd(II) and Pb(II) form stable 1:1 S_4 or S_3(N/O) complexes in $AztA^{aHbH}$, where a single metal ion bridges the two Cys-X_2-Cys sites from a- and b-MBDs or forms intermolecular a−a′ and b−b′ cross-linked structures. We hypothesize that these structures represent kinetically trapped intermediates that are poor substrates or regulators for metal transport by AztA.

MATERIALS AND METHODS

Plasmid Construction of Wild-Type and Mutant azt Operons and Metal Sensitivity Assays. The complete *azt* operon (*27*) was amplified from genomic DNA from the cyanobacterium *Anabaena* strain PCC 7120 and subcloned into pET3a (Novagen) between the *Bgl*II and *Eco*RI sites to create pETazt. A PCR-based quick-change method was employed for simultaneous substitution of Cys19 and Cys22 or Cys120 and Cys123 with Ser using pETazt as a template to create pETazt-C19S/C22S or pETazt-C120S/C123S, respectively. pETazt-C19S/C22S/C120S/C123S was prepared in an analogous fashion using pETazt-C19S/C22S as the PCR template. pETazt-Δ(1−105) was constructed by looping out the coding region for $AztA^{aH}$ using a PCR-based quick-change mutagenesis strategy with pETazt as the template. All plasmids were fully sequenced to verify their integrity. pETazt, pETazt-C19S/C22S, pETazt-C120S/C123S, pETazt-C19S/C22S/C120S/C123S, and pETazt-Δ(1−105) were transformed into *E. coli* GG48 (Δ*zitB*::Cm Δ*zntA*::Km) (*30*) and grown overnight at 37 °C in LB medium supplemented with 100 μg/mL ampicillin. Cultures were then diluted 1:50 into 10 mL of fresh LB/ampicillin medium supplemented with the indicated concentrations of metal salts, and the OD_{600} was recorded from duplicate or triplicate cultures as a function of time. For the metal concentration dependence, the OD_{600} was recorded following an 8−10 h incubation.

Purification of Recombinant $AztA^{aH}$ and $AztA^{aHbH}$ from E. coli. The regions encoding $AztA^{aH}$ (residues 1−105) and $AztA^{aHbH}$ (residues 1−213) were amplified by PCR from *Anabaena* PCC 7120 genomic DNA and cloned into pET3a (Novagen) between *Nde*I and *Eco*RI restriction sites to create pET3a-$AztA^{aH}$ and pET3a-$AztA^{aHbH}$, respectively. Plasmids encoding C19S/C22S $AztA^{aHbH}$ and C120S/C123S $AztA^{aHbH}$ were constructed from pET3a-$AztA^{aHbH}$ using PCR-based quick-change mutagenesis. All plasmids were transformed into *E. coli* BL21(DE3) and grown on LB to midlog phase and induced via addition of 0.4 mM IPTG. Freshly harvested cells were pelleted by low-speed centrifugation and suspended in 100 mL of buffer A [25 mM Tris-HCl, 3 mM DTT, 1 mM EDTA, and 80 mM imidazole (pH 6.0)] and lysed by sonication. The sonicated supernatant was subjected to HisTrapHP (Amersham Biosciences) chromatography (20 mL bed volume) on an Äkta-10 purifier, with elution achieved with a linear imidazole gradient (from 50 to 400 mM) in buffer B [25 mM Tris-HCl, 3 mM DTT, and 1 mM EDTA (pH 8.0)]. AztA MBD-containing fractions typically eluted between 125 and 175 mM imidazole, were pooled conservatively, and were further purified using Superdex 75 size-exclusion chromatography (*27*). Highly purified AztA MBD-containing fractions were pooled, concentrated, and dialyzed against 3 L of buffer C [5 mM MES-HCl and 0.20 M NaCl (pH 6.5)] in an anaerobic Vacuum Atmospheres glovebox. The purity of the final products was estimated by visualization of Coomassie-stained 18% Tricine−SDS−PAGE gels to be ≥90%. Uniformly ^{15}N-labeled $AztA^{aH}$ and $AztA^{aHbH}$ were purified in exactly the same way except that cells were grown on an M9 minimal medium, with $(^{15}NH_4)_2SO_4$ as the sole nitrogen source (*31*). The concentrations of wild-type $AztA^{aHbH}$, C19S/C22S (or C120C/C123S) $AztA^{aHbH}$, and $AztA^{aH}$ were determined using ϵ_{280} values of 11 180, 10 930, and 4845 M^{-1} cm^{-1}, respectively. All Cys residues in AztA domains were reduced as revealed by an anaerobic DTNB assay (*32*).

Cd(II) and Pb(II) Binding Experiments. Metal ion binding experiments with Cd(II) and Pb(II) were carried out anaerobically at ambient temperature (≈25 °C) as described previously (*27*) in either buffer C (for Cd) or buffer H [10 mM bis-Tris and 0.4 M NaCl (pH 7.0)] (for Pb). Metal binding isotherms were fit using DynaFit (*33*) as described previously (*34*) to 1:1 binding models with the total concentration of metal binding sites on AztA derivatives being an adjustable parameter.

Zn(II) Binding Experiments. Mag-fura-2 (Invitrogen M1290) ($K_{Zn} = 5.0 \times 10^7$ M^{-1}) (*35*) was employed in a Zn(II) competition assay with various AztA MBD fragments. Mag-fura-2 (7−10 μM) was mixed anaerobically with a known concentration of apoprotein (18−20 μM) in buffer C (*34*). The metal concentrations of each titrant were verified by atomic absorption spectroscopy, and the data were fit using a competitive binding model (DynaFit) (*33*, *34*) with K_{Zn} (mag-fura-2) and [mag-fura-2] as fixed parameters, and the

total concentration of Zn(II) binding sites on AztA derivatives as an adjustable parameter, to account for errors in pipetting, partial inactivation due to cysteine oxidation, or heterogeneity of metal sites. For $AztA^{aHbH}$, a two-site sequential binding model was used and defined by K_{Zn1} and K_{Zn2}, with the best-fit values of [$AztA^{aHbH}$] being 19.4 μM (20.0 μM input). For $AztA^{aH}$, a 1:1 binding model (K_{Zn}) was used with a best-fit [$AztA^{aH}$] of 9.1 μM (18.2 μM added). For C19S/C22S $AztA^{aHbH}$, a model assuming a mixture of two metal binding species with apparent affinities K_{Zn}^{A} and K_{Zn}^{B} was used, with best-fit [C19S/C22S $AztA^{aHbH-A}$] and [C19S/C22S $AztA^{aHbH-B}$] values of 9.9 μM each (20.0 μM total input), respectively. K_{Zn}^{A} reports on a 1:1 complex with the b-MBD, while K_{Zn}^{B} likely reports on an intermolecular b−b′ bridging species, analogous to the a−a′ bridging species that is observed for $AztA^{aH}$ (see Figure S1 of the Supporting Information).

NMR Spectroscopy. All NMR spectra were acquired on a Varian Unity Inova 600 MHz spectrometer in the Biomolecular NMR Laboratory at Texas A&M University. Sample preparation and subsequent metal additions were conducted in an anaerobic Vacuum Atmospheres glovebox at ambient temperature and incubated at least 2 h before the spectra were recorded. $^{1}H-^{15}N$ HSQC spectra were typically acquired using a 400 μM solution of uniformly ^{15}N-labeled $AztA^{aHbH}$ or $AztA^{aH}$ in buffer C [5 mM Mes and 0.20 M NaCl (pH 6.5)] at 25 °C. Sequential $^{1}H_N$, ^{15}N, $^{13}C\alpha$, and $^{13}C\beta$ resonance assignments of the a-MBD region were obtained using a 0.35 mM uniformly ^{15}N- and ^{13}C-labeled apo-$AztA^{aH}$ sample from analysis of $^{1}H-^{15}N$ HSQC, CBCA(CO)NH, and HNCACB experiments in buffer C containing 90% H_2O and 10% D_2O. NMR data were processed using NMRPipe and analyzed using Sparky, essentially as previously described (*31*). PREDICTOR (*36*) was used to analyze backbone $^{1}H_N$, ^{15}N, $^{13}C\alpha$, and $^{13}C\beta$ chemical shifts and sequence analysis to define the secondary structural segments in $AztA^{aH}$. The torsion angles (Ψ, Φ, and χ_1) of $AztA^{aH}$ predicted by PREDICTOR were found to be comparable to those experimentally determined in *Bacillus subtilis* CopZ (*37*).

NMR Analysis of Mixtures of [^{15}N]$AztA^{aH}$ and Unlabeled C19S/C22S $AztA^{aHbH}$. Zn_1-bound ^{15}N-labeled $AztA^{aH}$ (0.4 mM) incubated for 12 h in an anaerobic chamber was mixed with unlabeled C19S/C22S $AztA^{aHbH}$ at molar ratios of 1:1 and 1:1.5, and $^{1}H-^{15}N$ HSQC spectra were recorded within 2 h as described above.

X-ray Absorption Spectroscopy of Zn− and Cd−$AztA^{aH}$ Complexes. Samples of ≈1 mM $AztA^{aH}$ containing 0.7 molar equiv of Zn(II) or 0.5 molar equiv of Cd(II) were loaded into 10 μL wells of Lexan cuvets with 0.001 in. thick Kapton windows. Zn and Cd K edge X-ray absorption spectroscopic data were collected at the Stanford Synchrotron Radiation Laboratory on beamline 9-3 with the SPEAR3 ring operating at 3.0 GeV and 85−100 mA, with a fully tuned Si (220) LN_2-cooled monochromator, using a vertical aperture of 1 mm, and the upstream mirror set for harmonic rejection. Fluorescence excitation spectra were collected using a 30-element intrinsic Ge detector (Canberra) windowed to either Zn or Cd Kα emission. For Zn, a 6 μm Cu fluorescence filter backed by Soller slits was employed. The spectra shown in Figure 5 were averaged from six (Zn) and three (Cd) 21 min scans, and the data were reduced and analyzed using EXAFSPAK (http://www-ssrl.slac.stanford.edu/exafspak.html). Internal energy calibration defined the first inflection of Zn and Cd elemental standards as 9660.7 and 26714.0 eV, respectively. k values were calculated using threshold ($k = 0$) energies of 9670 and 26 720 eV, respectively.

RESULTS

The a- and b-MBDs Play Functionally Nonequivalent Roles in Zinc Resistance in E. coli. Previous studies of metal-sensing cyanobacterial operons regulated by ArsR family repressors suggest that these operons function similarly in *E. coli* and their original cyanobacterial hosts (*27*, *38*, *39*). To evaluate the degree to which individual MBDs are required to confer metal resistance in cell culture, we transformed the well-characterized Zn/Pb/Cd hypersensitive strain *E. coli* GG48 (Δ*zitB*, Δ*zntA*) (*30*), which lacks both known low- and high-affinity Zn/Cd efflux systems, with plasmids encoding the complete *Anabaena azt* operon in which one MBD or the other was inactivated by mutation. Figure 2A reveals that *E. coli* GG48 transformed with an *azt* operon in which the a-MBD was inactivated (C19S/C22S *azt*) is more sensitive to zinc toxicity at long incubation times (8−10 h) relative to GG48 transformed with an *azt* operon in which the b-MBD was inactivated (C120S/C123S *azt*). Analysis of the full growth curves for these strains measured in the presence of an intermediate concentration of Zn(II) (200 μM) reveals that this differential effect manifests itself at long incubation times (Figure 2C). In contrast, growth curves measured at highly toxic levels of Zn(II) (≥500 μM) (Figure 2E) reveal that while the b-MBD mutant retains a level of zinc resistance just below that of the wild-type operon, inactivation of the a-MBD confers a level of resistance only just above that of nontransformed cells. A similar level of resistance is obtained when both the a- and b-MBDs are inactivated compared to the a-MBD alone; this suggests that the a-MBD is largely capable of functioning independently of the b-MBD at high intracellular zinc loads. Unlike the case with Zn(II), inactivation of either the a- or the b-MBDs has only a small, but roughly equivalent, influence on Cd(II) resistance relative to the wild-type *azt* operon, with the double mutant only slightly more sensitive to high Cd(II) loads (25 μM) with long incubation times (Figure 2B,D,F). Thus, the presence of at least one functional MBD is sufficient to confer nearly wild-type, albeit modest (*27*), levels of Cd(II) resistance in these cells, a situation that appears to contrast with that of Zn(II).

The Two MBDs of AztA Have Different Zn(II) Binding Affinities. The in vivo metal resistance experiments described above make the prediction that individual MBDs might have distinct Zn(II) binding properties and that complexes formed with Zn(II) might be structurally different from those formed by Cd(II) and Pb(II). We first determined the stoichiometry and affinity of Zn(II) binding to various MBD-containing AztAs using a metal chelator competition assay. Here, the Zn(II) chelator mag-fura-2 (*34*) with a K_{Zn} of 5.0×10^7 M^{-1} (*35*) is mixed with purified AztA MBD-containing fragments and titrated with Zn(II) in an anaerobic atmosphere. The binding of Zn(II) to mag-fura-2 leads to a shift in the absorption maximum (from 366 to 325 nm). As shown in Figure 3A, the total concentration of Zn(II) required to saturate $AztA^{aHbH}$ (20 μM) and mag-fura-2 (9.7 μM) is ≈50 μM. This experiment reveals that $AztA^{aHbH}$ binds 2 molar equiv of Zn(II) with a K_{Zn} of $\geq 10^5$ M^{-1}. Quantitative

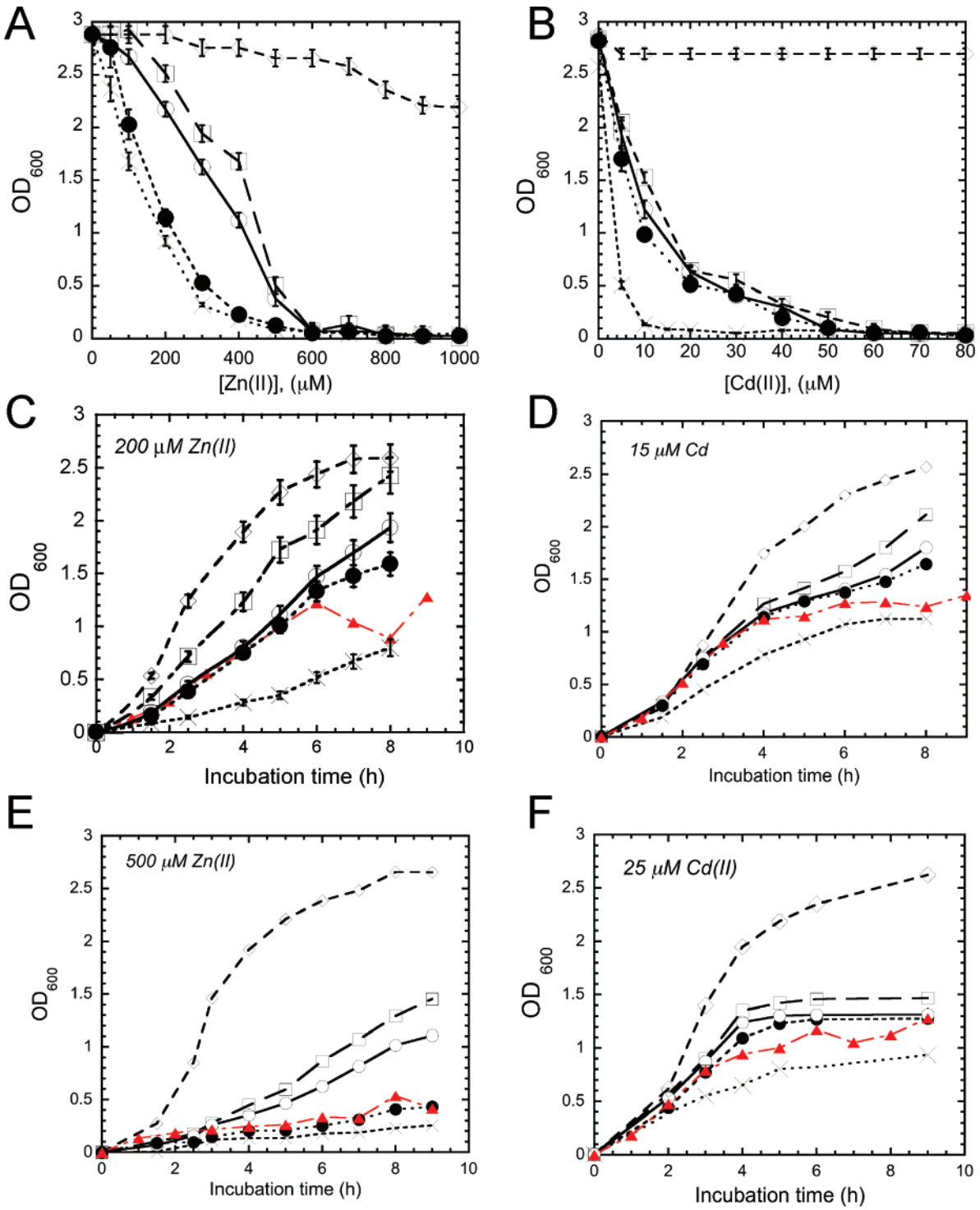

FIGURE 2: Zinc and cadmium resistance of Zn/Cd hypersensitive *E. coli* GG48 transformed with *azt* operons containing *aztA* metal binding missense mutations. Representative data were derived from duplicate or triplicate measurements for *E. coli* GG48 transformed with pET3a vector (X), pETazt-C19S/C22S/C120S/C123S (red triangles), pETazt-C19S/C22S (black circles), pETazt-C120S/C123S (white circles), and pETazt (white squares) relative to an isogenic wild-type W3100 strain (white diamonds).

curve fitting to a two-site binding model reveals that one Zn(II) binds to AztA^{aHbH} with an affinity far greater than that of mag-fura-2 [$K_{Zn1} = (9.4 \pm 1.0) \times 10^8$ M^{-1}], while the second binds with an affinity only slightly greater than that of mag-fura-2 [$K_{Zn2} = (8.0 \pm 0.6) \times 10^7$ M^{-1}]. The simplest interpretation of this experiments is that each MBD of AztA^{aHbH} binds 1 molar equiv of Zn(II) with measurably different affinities. If the His-rich linker segments in AztA^{aHbH} bind Zn(II), these sites are characterized by an affinity K_{Zn} of $\leq 10^5$ M^{-1} or far weaker than that of mag-fura-2, since they are not observed in this assay.

To determine which MBD (a or b) binds Zn(II) more tightly, we performed parallel competition experiments with AztA^{aH} (Figure 3B), which contains only the a-MBD and the His-rich region, and C19S/C22S AztA^{aHbH} (Figure 3C), which contains a wild-type b-MBD and both His-rich

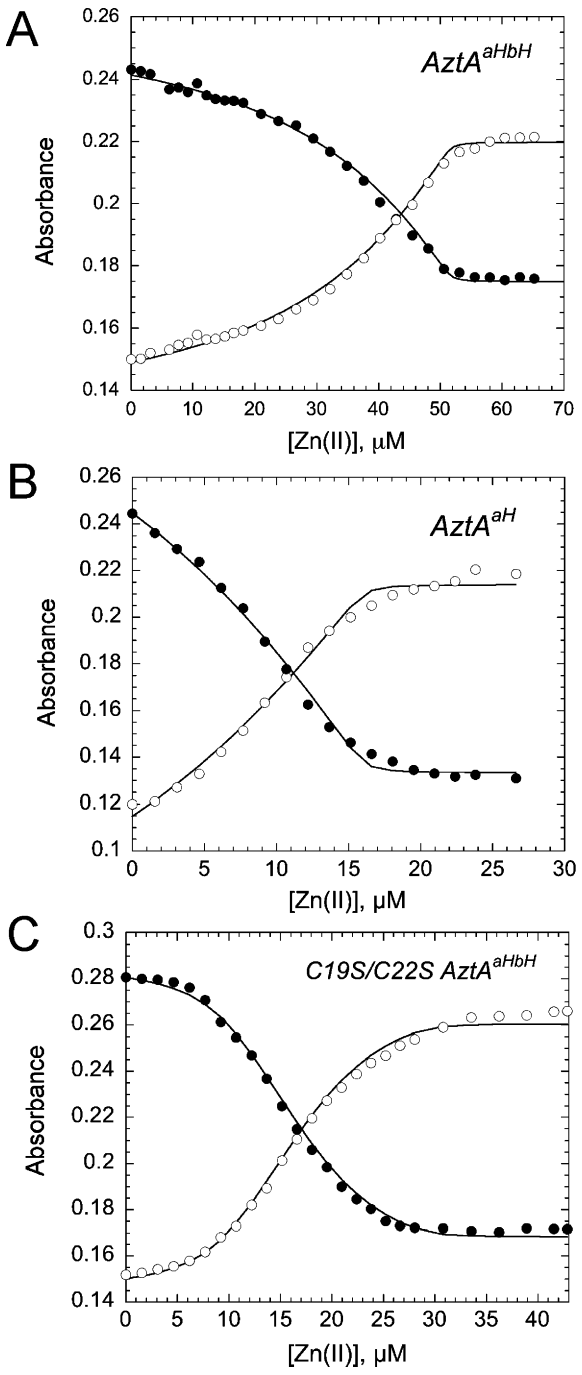

FIGURE 3: Representative anaerobic titrations of Zn(II) into a mixture of mag-fura-2 and purified AztA^{aHbH} (A), AztA^{aH} (B), or C19S/C22S AztA^{aHbH} (C) in buffer C [5 mM Mes and 0.2 M NaCl (pH 6.5)]. For panel A, mag-fura-2 (10.0 μM) and AztA^{aHbH} (20.0 μM) were used. For panel B, 7.0 μM mag-fura-2 was mixed with 18.2 μM Azt^{aH}. For panel C, 10.0 μM mag-fura-2 was mixed with 20.0 μM C19S/C22S AztA^{aHbH}. The absorbance changes at 366 (●) and 325 nm (○) were monitored and plotted as a function of total Zn(II) concentration. The solid lines represent a simultaneous, nonlinear, least-squares fitting curve generated by Dynafit to 2:1 stepwise binding models (defined by K_{Zn1} and K_{Zn2}; see the text) for AztA^{aHbH}, a 1:1 model for AztA^{aH} [$K_{Zn} = (9.3 \pm 1.5) \times 10^7$ M^{-1}], and an equimolar mixture of sites model for C19S/C22S AztA^{aHbH} [see Materials and Methods; $K_{Zn}^{A} = (8.4 \pm 2.8) \times 10^8$ M^{-1}, and $K_{Zn}^{B} = (7.4 \pm 1.2) \times 10^6$ M^{-1}] with K_{Zn} (mag-fura-2) fixed at 5.0×10^7 M^{-1}.

domains. As one can see, the added Zn(II) binds to AztA^{aH} and mag-fura-2 with approximately equal affinity until saturation of the available sites occurs, with a K_{Zn} of $(9.3 \pm 1.5) \times 10^7$ M^{-1}, or comparable to that of the low-affinity binding site in intact AztA^{aHbH} (Figure 3B). In contrast, there is a clear plateau in the early region of the titration curve for C19S/C22S AztA^{aHbH} (Figure 3C) like that for intact AztA^{aHbH}, with a K_{Zn} of $(8.4 \pm 2.8) \times 10^8$ M^{-1} or comparable to that of the high-affinity site in wild-type AztA^{aHbH} (Figure 3A). These data reveal that each of the two MBDs of AztA^{aHbH} harbors a Zn(II) binding site and that the affinity of Zn(II) for the N-terminal a-MBD is lower by a factor of 5−10 than that for the C-terminal b-MBD.

Cd(II) and Pb(II) Form Inter- and Intramolecularly Bridging Structures. Cd(II) was shown to be a strong inducer of *aztA* expression in *Anabaena* but confers little resistance to Cd(II) salts in *E. coli* (*27*). The UV−visible absorption spectra of AztA^{aHbH} titrated with Cd(II) show the formation of a stoichiometric 1:1 Cd(II)−AztA^{aHbH} complex (Figure 4A, inset), in contrast to that obtained with Zn(II) (Figure 3). The intense absorption at ≈240 nm can be attributed to $S^- \rightarrow$ Cd(II) ligand-to-metal charge transfer transitions with an ϵ_{240} of ≈5000−6000 M^{-1} cm^{-1} expected per Cd−S bond (*40*, *41*). The molar absorptivity of the 1:1 Cd(II)−AztA^{aHbH} complex is 19 000 M_{Cd}^{-1} cm^{-1} (Figure 4A), a value consistent with three to four cysteine thiolate ligands. This result suggests that a single Cd(II) ion bridges both MBDs in intact AztA^{aHbH}, an interpretation supported by sedimentation equilibrium experiments (see below).

In contrast, the single a-MBD-containing AztA^{aH} binds only 0.5 molar equiv of Cd(II) at saturation (Figure 4A, inset), with a molar absorptivity ϵ_{240} of 11 000 M_{Cd}^{-1} cm^{-1}, or approximately one-half of that of AztA^{aHbH}; this suggests that a single Cd(II) ion forms an intermolecular S_4 complex between two AztA^{aH} domains. The same stoichiometry and molar absorptivity characterize the C19S/C22S AztA^{aHbH} complex (Figure 4A). Similar trends are observed for Pb(II) (Figure 4B). Two $S^- \rightarrow$ Pb(II) LMCT transitions are observed for Pb(II)-saturated AztA^{aHbH} with the molar absorptivities and energies of these absorption bands most consistent with approximately three thiolate ligands to the Pb(II) ion (*27*, *42*−*44*).

The assembly states of Zn_1-, Zn_2-, Cd_1-, and Pb_1-substituted AztA^{aHbH} are all described well by a single-ideal species molecular mass of ≈24 kDa in all cases, consistent with monomeric AztA^{aHbH} (Table SI of the Supporting Information). Thus, the Cys-thiolate-rich Cd_1 and Pb_1 complexes are best described as intramolecularly bridging chelates that cross-link the a- and b-MBDs. In contrast, size exclusion chromatography analysis of apo versus Zn_1 and $Cd_{0.5}$ forms of AztA^{aH} (Figure S1) reveals that while the apparent molecular masses of apo-AztA^{aH} and Zn_1-bound AztA^{aH} are mostly monomeric (≈12 kDa), addition of 0.5 molar equiv of Cd(II) gives rise to an ≈23 kDa dimeric species. These results are consistent with parallel dynamic light scattering experiments (Figure S1). Thus, Cd(II) readily mediates intermolecular a−a′ cross-linking of a-MBDs between AztA^{aH} molecules, in contrast to Zn(II).

X-ray Absorption Spectroscopy of Zn(II)- and Cd(II)-Bound AztA^{aH}. K-Edge X-ray absorption spectroscopy (XAS) was employed to further investigate the Zn(II) and Cd(II) metal−ligand donor sets. Cd K-edge X-ray absorption spectroscopic analysis of the Cd(II)−AztA^{aH} complex indicates a coordination environment consisting primarily of sulfur scatterers at 2.50 Å (Figure 5A). The data are most

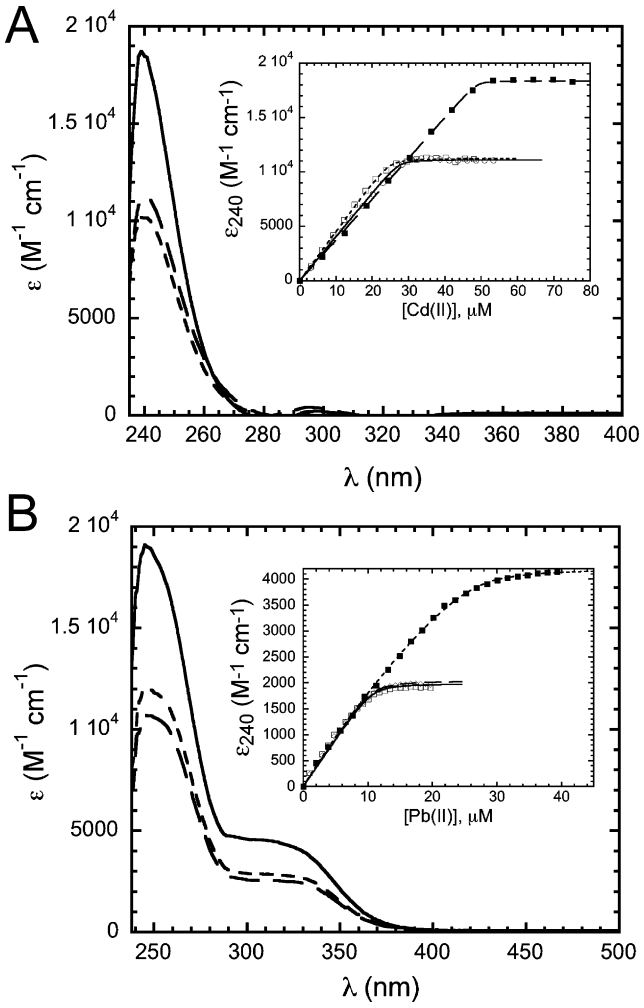

FIGURE 4: (A) Optical absorption spectra of 1:1 Cd(II)-saturated AztA^{aHbH} (—), 0.5:1 Cd(II)-saturated AztA^{aH} (- - -), and 0.5:1 Cd-(II) saturated C19S/C22S AztA^{aHbH} (— — —). The inset shows anaerobic Cd(II)−AztA binding isotherms {ϵ_{240} vs total [Cd(II)], 50 μM protein} generated from the optical spectra of AztA^{aHbH} (■), AztA^{aH} (□), and C19S/C22S AztA^{aHbH} (○). The smooth curve drawn through the data points reflects a K_{Cd} of $>5 \times 10^7$ M^{-1}, a lower limit given the high protein concentration that was used. (B) Optical absorption spectra of 1:1 Pb(II)-saturated AztA^{aHbH} (—), 0.5:1 Pb(II)-saturated AztA^{aH} (- - -), and 0.5:1 Pb(II)-saturated C19S/C22S AztA^{aHbH} (— — —). The inset shows anaerobic binding isotherms {ϵ_{320} vs total [Pb(II)], 20 μM protein} generated from the optical spectra of AztA^{aHbH} (■), AztA^{aH} (□), and C19S/C22S AztA^{aHbH} (◇) obtained upon titration of Pb(II). For AztA^{aHbH}, the solid line represents a least-squares fitted curve with a K_{Pb} of 8.0 $\times 10^7$ M^{-1}. For AztA^{aH} and C19S/C22S AztA^{aHbH}, the smooth curve reflects a lower limit for a K_{Pb} of $\geq 1 \times 10^8$ M^{-1}.

consistent with an average Cd(II)S$_3$(O/N) coordination complex (Table SII of the Supporting Information). In contrast, curve fitting of EXAFS obtained for equilibrium Zn(II)$_{0.7}$−AztA^{aH} complexes reveals a Zn(II)S$_2$(N/O)$_2$ coordination environment, a finding consistent with coordination by Cys19 and Cys22 and possibly Asp18, as reported in *E. coli* ZntA (*19*), with a water molecule completing the tetrahedral chelate structure (Figure 5B and Table SII).

NMR Studies of Zn(II)-, Cd(II)-, and Pb(II)-Bound AztA^{aHbH}. Since Zn(II) and Cd(II)/Pb(II) bind to AztA^{aHbH} with different stoichiometries and coordination structures, we next examined the nature of the structural changes by NMR spectroscopy in an attempt to correlate these changes to the

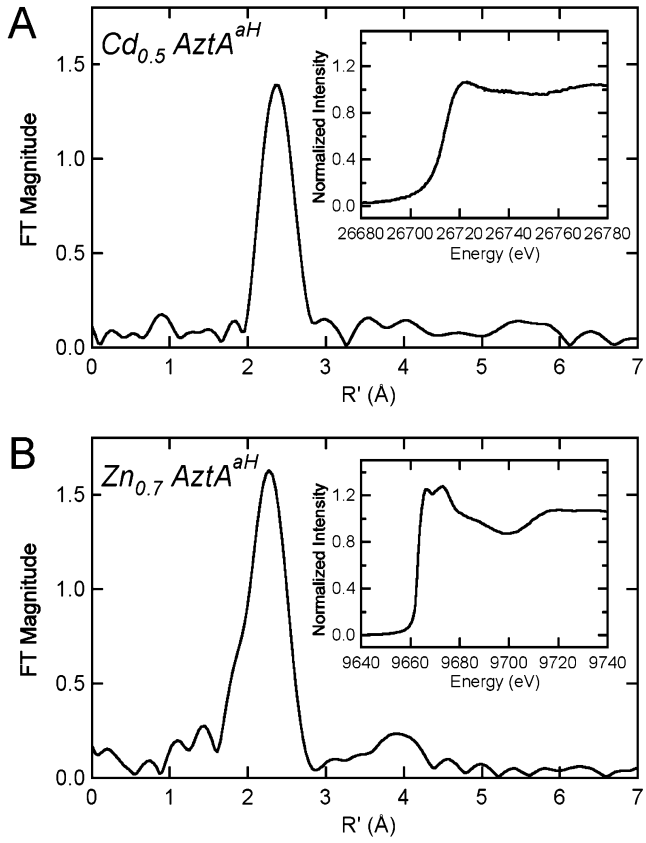

FIGURE 5: EXAFS analysis of Zn(II)- and Cd(II)-bound AztA^{aH}. (A) Fourier transform (k = 2−12 Å^{-1}; k^3 weighting) of the Cd K-edge EXAFS of the Cd(II)$_{0.5}$−AztA^{aH} complex. (B) Fourier transform (k = 2−12 Å^{-1}; k^3 weighting) of the Zn K-edge EXAFS of the Zn(II)$_{0.7}$−AztA^{aH} complex. Cadmium and zinc K-edge X-ray absorption near-edge spectra are shown in the insets of panels A and B, respectively. Parameters that define the best fits to these data are compiled in Table SII.

specificity of metal transport by AztA. We recorded two-dimensional ^{1}H−^{15}N HSQC spectra of AztA^{aHbH} in the absence and presence of 1 and 2 molar equiv of Zn(II) versus saturating 1:1 Cd(II) and Pb(II) and compared these spectra to those of apo and Zn$_1$-bound AztA^{aH} (Figure 6). Inspection of the ^{1}H−^{15}N HSQC spectra acquired for apo-AztA^{aHbH} (Figure 6B) versus those for apo-AztA^{aH} (Figure 6A, blue contours) reveals that of the two MBDs of AztA^{aHbH}, only the N-terminal a-MBD gives well-resolved resonances of relatively uniform intensity; in contrast, the expected resonances for the C-terminal b-MBD are of significantly lower intensity and, in some cases, missing altogether (Figure S2 of the Supporting Information). Intermediate (microsecond to millisecond) exchange on the ^{1}H NMR time scale between two or more conformations seems a likely origin of resonance broadening, a characteristic not unprecedented from NMR studies of other Atx1-like MBDs (*45*).

Complete ^{1}H$_N$ and ^{15}N, ^{13}Cα, and ^{13}Cβ assignments were obtained for apo-AztA^{aH} from Ser6 to Gln75, with the exception of Leu30, and Asp18, Cys19, and Ser21 in the metal binding loop (Table SIII of the Supporting Information). A comparison of the amide chemical shifts of the a-MBD in the context of AztA^{aH} versus AztA^{aHbH} shows that they are virtually identical in the apo state (Figures S2 and S3), consistent with little interaction between the a- and b-MBDs in the two-domain AztA^{aHbH} molecule. Chemical

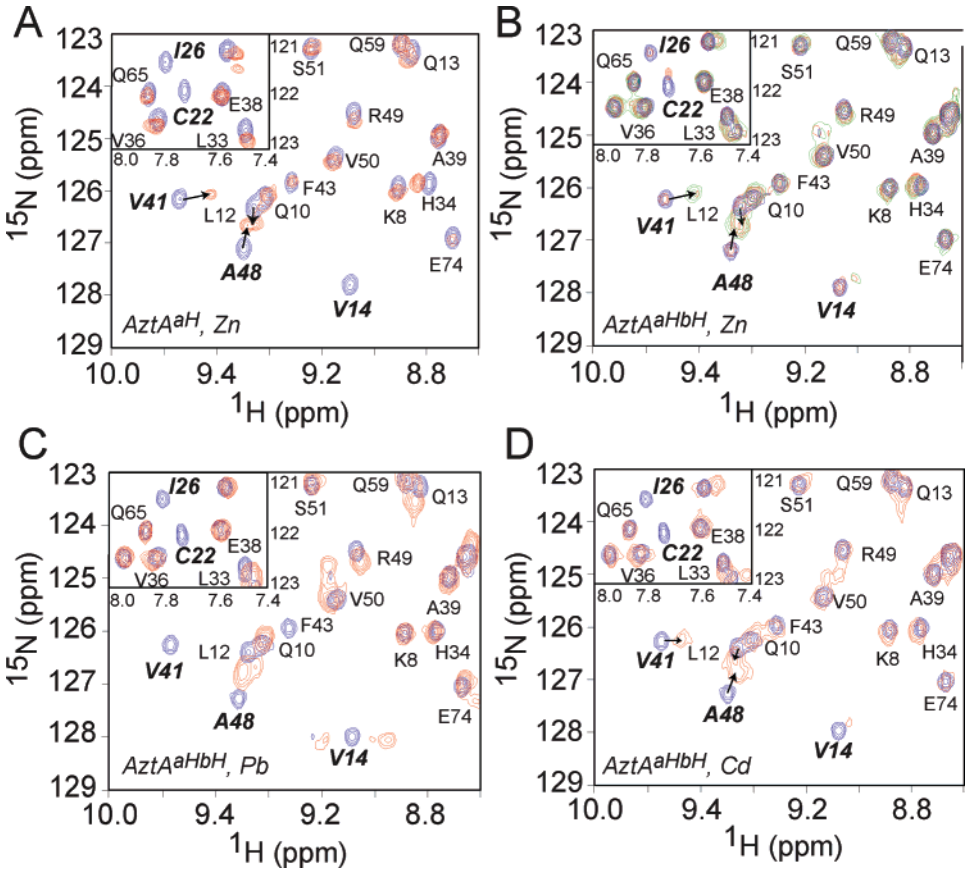

FIGURE 6: Superposition of selected regions of the ^{1}H−^{15}N HSQC spectra of (A) apo-AztA^{aH} (blue cross-peaks) and apo-AztA^{aH} with 1 molar equiv of Zn(II) (red contours), (B) apo-AztA^{aHbH} (blue contours) mixed with 1 molar equiv of Zn(II) (red contours) and 2 molar equiv of Zn(II) (green contours), (C) apo-AztA^{aHbH} (blue contours) mixed with 1 molar equiv of saturating Cd(II) (red contours), and (D) apo-AztA^{aHbH} (blue contours) mixed with 1 molar equiv of saturating Pb(II) (red contours). Note that the movement of the Val41 and Ala48 cross-peaks in the $\beta2-\beta3$ loop in the AztA^{aHbH} spectrum (panel B) is maximal only when both the a- and b-MBDs are filled with Zn; in contrast, this perturbation appears to be maximal with only 1 molar equiv of Cd and Pb (panels C and D). In the insets, extensive line broadening of both Cys22 and Ile26 is also reporting on the metal occupancy of the DCXXC region in the a-MBD.

shift indexing using PREDICTOR (*36*) is consistent with the expected $\beta\alpha\beta\beta\alpha\beta$ topology (*10*), with secondary structural segments encompassing approximately residues 7−15 ($\beta1$), 22−31 ($\alpha1$), 37−42 ($\beta2$), 47−53 ($\beta3$), 59−67 ($\alpha2$), and 71−74 ($\beta4$) (see Figure 1B). Binding of Zn(II) to AztA^{aH} induces significant chemical shift perturbations in the metal binding loop region, flanking residues in the $\beta1$ strand and $\alpha1$ helix, and the $\beta2-\beta3$ loop in the proximity of the metal binding loop (Figure 6A and Figure S3). In the spectral region that is shown, Val14, Cys22, and Ile26 in the metal binding loop and Val41 and Ala48 in the $\beta2-\beta3$ loop region are good reporters of metal binding by the a-MBD.

A comparison of the changes in the spectra of apo-AztA^{aHbH} upon addition of 1 (red contours) versus 2 (green contours) molar equiv of Zn(II) reveals that the addition of the first molar equivalent of Zn(II) induces very little perturbation in the amide groups of the a-MBD, consistent with the relative affinities of the two MBDs for Zn(II) (Figure 3). Upon addition of the second molar equivalent of Zn(II), we see significant perturbations in the a-MBD within AztA^{aHbH} (Figure 6B), analogous to those changes observed upon addition of Zn(II) to AztA^{aH} (Figure 6A). In contrast, addition of a stoichiometric amount of Cd(II) (Figure 6D) or Pb(II) (Figure 6C) induces perturbations of the a-MBD resonances qualitatively analogous to those observed upon addition of Zn(II) to AztA^{aH}, with Cys22, Ile26, and Val41 reporting most strongly on these changes (Figure 6A). Note that these spectral changes do not allow us to easily discriminate between monomolecular a-MBD and interdomain a-b MBD metal-cross-linked species since we can observe changes in only a-MBD resonances. Nonetheless, these data are consistent with formation of an a-MBD−b-MBD site-bridging complex in Cd_1− and Pb_1−AztA^{aHbH} complexes that is structurally distinct from that in the Zn_1 and Zn_2 complexes.

Facile Transfer of Zn(II) from the a-MBD to the b-MBD. Since the b-MBD has a higher equilibrium affinity for Zn(II) relative to the N-terminal a-MBD, this finding makes the prediction that Zn(II) bound to the a-MBD should be capable of transferring to the b-MBD on thermodynamic grounds, provided the energy barrier between the two states is small. To test this idea, we incubated Zn(II)-complexed, ^{15}N-labeled AztA^{aH} (red contours) with unlabeled apo-C19S/C22S AztA^{aHbH} at a ratio of 1:1 (blue contours) and monitored metal occupancy of the a-MBD by ^{1}H−^{15}N HSQC spectroscopy (Figure 7). These data show that the apo b-MBD is capable of stripping the Zn(II) prebound to the a-MBD, given the appearance of apo state resonance frequencies for Cys22, Ile26, and Val41 in ^{15}N-labeled AztA^{aH}, among others. The transfer efficiency estimated by the relative peak intensities of Zn(II) versus apo state cross-peaks for Val41 suggests that ≥80% of the Zn(II) moved

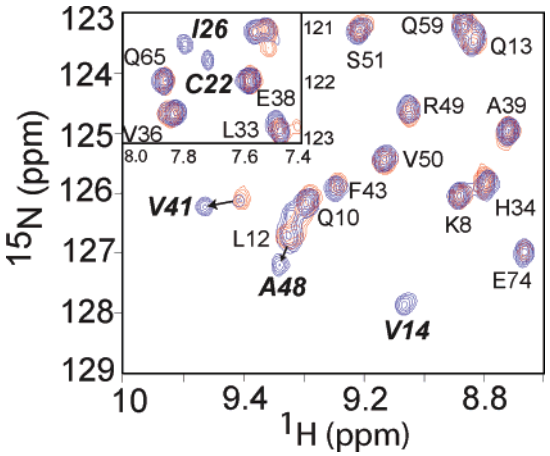

FIGURE 7: Transfer of Zn(II) from Zn(II)-loaded uniformly ^{15}N-labeled AztA^{aH} to unlabeled apo-C19S/C22S AztA^{aHbH}. Superposition of ^{1}H−^{15}N HSQC spectra of a 1:1 complex of Zn(II) and AztA^{aH} alone (red contours) or in the presence of unlabeled apo-C19S/C22S AztA^{aHbH} at a 1:1 molar ratio (blue contours). Note that resonances corresponding to Val14, Cys22, Ile26, Val41, and Ala48 return to their characteristic positions in apo-AztA^{aH} upon addition of a stoichiometric amount of apo-b-MBD, indicative of Zn(II) transfer. In the inset, extensive line broadening of both Cys22 and Ile26 also reports on the metal occupancy of the DCXXC region in the a-MBD.

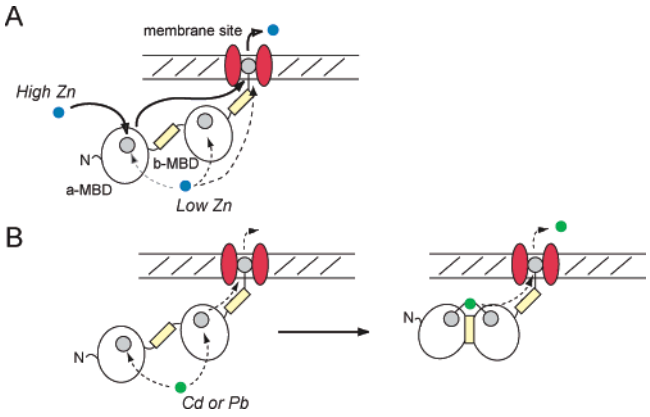

FIGURE 8: Hypothetical model that illustrates plausible pathways for the transfer of (A) Zn or (B) Cd/Pb from the cytosolic MBD region of AztA to the transmembrane site, and on to the other side of the membrane, consistent with the data presented here. At low cytosolic Zn loads, the metal can interact with the a-MBD, b-MBD, or transmembrane site in a manner dictated by their relative affinities. At high intracellular Zn loads, metal interacts with the low-affinity a-MBD to maximally stimulate the transporter. For Cd/Pb, these ions form a trapped inter-MBD complex. Metal binding sites are indicated by the filled gray circles, within the a-MBD, b-MBD, and the transmembrane sites indicated (*49*). The contribution of the His-rich domains (yellow rectangles) to Zn(II) transport is not yet known; however, they likely bind Zn(II) (*61*) and may well influence rates of transport of metal through the membrane.

from the a-MBD in AztA^{aH} to the b-MBD in C19S/C22S AztA^{aHbH} under these conditions, a finding roughly consistent with their relative affinities.

DISCUSSION

How N-terminal MBDs influence metal transport by the divalent metal ion-specific P_{1B}-type ATPases is not fully understood. In simple Zn/Cd/Pb-specific P_{1B}-type ATPases, e.g., *E. coli* ZntA, kinetic studies reveal that the single N-terminal MBD enhances the steady state ATPase activity (*46*) and overall turnover of the enzyme, either by increasing the rate of metal binding, which is fast ($\approx 10^8$ M^{-1} s^{-1}) (*47*), or by stimulating the release of metal ion from the transmembrane site, which is rate-limiting for transport (*17*). Our studies with *Anabaena* AztA provide new insights into how tandemly linked MBDs in a divalent metal transporter might bias the metal specificity of the efflux pump more toward Zn(II), relative to abiological Cd(II) and Pb(II) ions, in a way that is not achievable with a single MBD. They further suggest that the trend toward increasing numbers of MBDs found in mammalian copper-specific transporters might have been used to fine-tune the intrinsic metal selectivity and transport efficiency of the pump beyond that which was possible with no or one MBD.

Consistent with previous studies, neither MBD is absolutely essential for mediating metal resistance and, by extension, metal efflux through the AztA transporter (*48*). However, they do suggest that the low-affinity a-MBD serves a specialized regulatory role under high intracellular zinc loads in a manner that appears to be largely independent of the b-MBD (Figure 2). Perhaps only under these conditions would the low-affinity N-terminal a-MBD be capable of binding Zn(II) in the cell, which would then quickly move via simple mass action (dissociation and/or reassociation) or direct transfer via metal−ligand exchange to the membrane proximal b-MBD (Figure 7) or the transmembrane site itself (see Figure 8A) on thermodynamic grounds, given the higher affinity of each for Zn(II) relative to the a-MBD (Figure 3) (*49*). However, it is important to emphasize that it has not yet been shown that Zn(II) is capable of moving from the a-MBD to either site directly within the same polypeptide chain, nor has the affinity of the transmembrane site for Zn(II) in AztA been experimentally determined. Although inter-MBD copper transfer has also been observed among the MBDs in ATP7B, as well as intermolecular transfer between Hah1 and select MBDs in both ATP7A and ATP7B (*12*, *50*, *51*), our data do not support a model of an obligatory transfer from the a-MBD to the b-MBD since inactivation of the b-MBD alone mediates a level of Zn(II) resistance that is nearly as effective as that of the wild-type MBD.

In contrast to the situation with Zn(II), the more thiophilic Cd(II) and Pb(II) ions appear to form kinetically stable inter- and intramolecularly bridged metal complexes in AztA (Figures 3−5), analogous to those observed previously for Cd(II)-bound CadA from *L. monocytogenes* (*20*) and metalated copper chaperones (*14*, *25*, *52*) (Figure 8B). Furthermore, this intramolecularly bridged metal complex in AztA^{aHbH} may be electrostatically stabilized as well, due to the anticipated complementary surface potentials of the a- and b-MBDs, with the a-MBD characterized by a small positive patch contributed by the β3 strand with the b-MBD exhibiting a strongly negative surface potential on the α3−β4 face of the domain (Figure S5 of the Supporting Information). The Cd(II) and Pb(II) complexes thus formed may not be a strong allosteric modulator of the ATPase activity relative to the Zn(II) complex, thus providing a means of biasing the metal selectivity of the efflux pump toward Zn(II).

Anabaena AztA, like the closely related *Synechocystis* ZiaA (*53*), likely transports Zn(II) from the cytoplasm to the periplasm. The periplasm is known to be important for metal ion partitioning and homeostasis, and this is particularly

so for cyanobacteria which have unusual requirements for iron, copper, and manganese to supply the photosynthetic machinery with metal cofactors, as well as for other metal ions such as Zn, Co, and Mo (*54*). This compartment contains several metal-specific solute binding proteins, including *Synechocystis* ZnuA (Zn-specific) (*55*) and FutA2 (Fe^{III}-specific) (*56*) and *Anabaena* AzuA (likely Zn-specific) (*27*) that could function in metal storage and homeostasis of essential transition ions, and at high intracellular loads, in detoxification. *Anabaena*, like other cyanobacteria such as *Oscillatoria brevis* (*57*) and *Synechococcus* (*58*), is known to encode a metallothionein that efficiently sequesters divalent metals in the cytoplasm (*59*). Cd binds to *Synechococcus* SmtA avidly and is readily capable of displacing three of its four bound Zn ions (*60*). *Anabaena* and other cyanobacteria may have evolved partially overlapping or redundant detoxification and storage systems for zinc in a manner that maintains an optimal response to abiological Cd and Pb.

Finally, although similar His-rich sequences have been identified in other Zn/Cd-specific P_{1B}-type ATPases (*53*, *57*), the functional role of these regions C-terminal to both the a- and b-MBDs in AztA requires further study. Blast analysis against the complete plant and bacterial genome databases suggests that an AztA-like domain organization of a canonical MBD followed by a His-rich segment in predicted metal-transporting ATPases is not unique and can be found in most classes of bacteria, including Proteobacteria, Firmicutes, Bacteroidetes, and Cyanobacteria, in addition to *Arabidopsis*. Clearly, the His-rich region between residue ≈77 and 105 in $AztA^{aH}$ is unstructured and/or conformationally dynamic since sequential assignments for most of these resonances could not be obtained due to resonance overlap or conformation exchange broadening (Figure S4). However, addition of a stoichiometric amount of Zn(II) to $AztA^{aH}$ results in movement and chemical exchange broadening of at least a subset of these resonances which is largely paralleled by chemical shift perturbations in the metal binding and $\beta2-\beta3$ loops within the folded domain (Figure 6). The simplest interpretation of these spectral changes is that the bound Zn(II) is in intermediate exchange between sites, despite the fact that the His-rich linker binds Zn(II) with an apparent affinity that is weaker than even that of the a-MBD, since mutagenesis of the Cys pair in individual MBDs abrogates high-affinity ($K_{Zn} \geq 5 \times 10^5\ M^{-1}$) metal binding (Figure 3). Binding of metal to these His-rich domains may enhance the on-rate and/or facilitate the transfer of metal between MBDs and the b-MBD and intramembrane sites. Consistent with this, preliminary findings reveal that incubation with antisera raised against the His-rich sequence in Bxa1, a closely related CPx-ATPase from the cyanobacterium *O. brevis* (*39*), significantly decreases the ATPase activity of Bxa1 in vitro (T. Liu, unpublished results). Detailed kinetic studies of metal binding will be required to understand the mechanistic role that these domains play in stimulation of ATPase activity and metal transport across membranes.

ACKNOWLEDGMENT

We thank Dr. Xiangming Kong for help in acquiring the NMR data, Dr. Xiaohua Chen and Mr. Zhen Ma for assistance in analyzing the metal titration data, and Dr. Xiaohua Chen for constructing plasmids used in this work.

SUPPORTING INFORMATION AVAILABLE

Tables of sedimentation equilibrium, EXAFS curve fitting results, and resonance assignments; HPLC size exclusion chromatographic analysis, HSQC spectra, chemical shift difference plots, and electrostatic surface potential renderings of homology models; and supplementary methods. This material is available free of charge via the Internet at http://pubs.acs.org.

REFERENCES

1. Lutsenko, S., and Kaplan, J. H. (1995) Organization of P-type ATPases: Significance of structural diversity, *Biochemistry 34*, 15607−15613.
2. Arguello, J. M. (2003) Identification of ion-selectivity determinants in heavy-metal transport P_{1B}-type ATPases, *J. Membr. Biol. 195*, 93−108.
3. Arnesano, F., Banci, L., Bertini, I., Ciofi-Baffoni, S., Molteni, E., Huffman, D. L., and O'Halloran, T. V. (2002) Metallochaperones and metal-transporting ATPases: A comparative analysis of sequences and structures, *Genome Res. 12*, 255−271.
4. Bartee, M. Y., and Lutsenko, S. (2007) Hepatic copper-transporting ATPase ATP7B: Function and inactivation at the molecular and cellular level, *Biometals 20*, 627−637.
5. Williams, L. E., and Mills, R. F. (2005) P(1B)-ATPases: An ancient family of transition metal pumps with diverse functions in plants, *Trends Plant Sci. 10*, 491−502.
6. Dutta, S. J., Liu, J., Hou, Z., and Mitra, B. (2006) Conserved aspartic acid 714 in transmembrane segment 8 of the ZntA subgroup of P1B-type ATPases is a metal-binding residue, *Biochemistry 45*, 5923−5931.
7. Sazinsky, M. H., Agarwal, S., Arguello, J. M., and Rosenzweig, A. C. (2006) Structure of the Actuator Domain from the *Archaeoglobus fulgidus* Cu^+-ATPase, *Biochemistry 45*, 9949−9955.
8. Sazinsky, M. H., Mandal, A. K., Arguello, J. M., and Rosenzweig, A. C. (2006) Structure of the ATP binding domain from the *Archaeoglobus fulgidus* Cu^+-ATPase, *J. Biol. Chem. 281*, 11161−11166.
9. Dmitriev, O., Tsivkovskii, R., Abildgaard, F., Morgan, C. T., Markley, J. L., and Lutsenko, S. (2006) Solution structure of the N-domain of Wilson disease protein: Distinct nucleotide-binding environment and effects of disease mutations, *Proc. Natl. Acad. Sci. U.S.A. 103*, 5302−5307.
10. Rosenzweig, A. C., and O'Halloran, T. V. (2000) Structure and chemistry of the copper chaperone proteins, *Curr. Opin. Chem. Biol. 4*, 140−147.
11. Walker, J. M., Huster, D., Ralle, M., Morgan, C. T., Blackburn, N. J., and Lutsenko, S. (2004) The N-terminal metal-binding site 2 of the Wilson's Disease Protein plays a key role in the transfer of copper from Atox1, *J. Biol. Chem. 279*, 15376−15384.
12. Achila, D., Banci, L., Bertini, I., Bunce, J., Ciofi-Baffoni, S., and Huffman, D. L. (2006) Structure of human Wilson protein domains 5 and 6 and their interplay with domain 4 and the copper chaperone HAH1 in copper uptake, *Proc. Natl. Acad. Sci. U.S.A. 103*, 5729−5734.
13. Banci, L., Bertini, I., Cantini, F., Felli, I. C., Gonnelli, L., Hadjiliadis, N., Pierattelli, R., Rosato, A., and Voulgaris, P. (2006) The Atx1-Ccc2 complex is a metal-mediated protein-protein interaction, *Nat. Chem. Biol. 2*, 367−368.
14. Banci, L., Bertini, I., Ciofi-Baffoni, S., Kandias, N. G., Robinson, N. J., Spyroulias, G. A., Su, X. C., Tottey, S., and Vanarotti, M. (2006) The delivery of copper for thylakoid import observed by NMR, *Proc. Natl. Acad. Sci. U.S.A. 103*, 8320−8325.
15. Pufahl, R. A., Singer, C. P., Peariso, K. L., Lin, S. J., Schmidt, P. J., Fahrni, C. J., Culotta, V. C., Penner-Hahn, J. E., and O'Halloran, T. V. (1997) Metal ion chaperone function of the soluble Cu(I) receptor Atx1, *Science 278*, 853−856.
16. Rae, T. D., Schmidt, P. J., Pufahl, R. A., Culotta, V. C., and O'Halloran, T. V. (1999) Undetectable intracellular free copper: The requirement of a copper chaperone for superoxide dismutase, *Science 284*, 805−808.

17. Mandal, A. K., and Arguello, J. M. (2003) Functional roles of metal binding domains of the *Archaeoglobus fulgidus* Cu^{+}-ATPase CopA, *Biochemistry 42*, 11040−11047.
18. Borrelly, G. P., Rondet, S. A., Tottey, S., and Robinsn, N. J. (2004) Chimeras of P-type ATPases and their transcriptional regulators: Contributions of a cytosolic amino-terminal domain to metal specificity, *Mol. Microbiol. 53*, 217−227.
19. Banci, L., Bertini, I., Ciofi-Baffoni, S., Finney, L. A., Outten, C. E., and O'Halloran, T. V. (2002) A new zinc-protein coordination site in intracellular metal trafficking: Solution structure of the Apo and Zn(II) forms of ZntA(46−118), *J. Mol. Biol. 323*, 883−897.
20. Banci, L., Bertini, I., Ciofi-Baffoni, S., Su, X. C., Miras, R., Bal, N., Mintz, E., Catty, P., Shokes, J. E., and Scott, R. A. (2006) Structural basis for metal binding specificity: The N-terminal cadmium binding domain of the P1-type ATPase CadA, *J. Mol. Biol. 356*, 638−650.
21. Finney, L. A., and O'Halloran, T. V. (2003) Transition metal speciation in the cell: Insights from the chemistry of metal ion receptors, *Science 300*, 931−936.
22. Chen, K., Yuldasheva, S., Penner-Hahn, J. E., and O'Halloran, T. V. (2003) An atypical linear Cu(I)-S2 center constitutes the high-affinity metal-sensing site in the CueR metalloregulatory protein, *J. Am. Chem. Soc. 125*, 12088−12089.
23. Ralle, M., Lutsenko, S., and Blackburn, N. J. (2003) X-ray absorption spectroscopy of the copper chaperone HAH1 reveals a linear two-coordinate Cu(I) center capable of adduct formation with exogenous thiols and phosphines, *J. Biol. Chem. 278*, 23163−23170.
24. Banci, L., Bertini, I., Ciofi-Baffoni, S., Su, X. C., Borrelly, G. P., and Robinson, N. J. (2004) Solution structures of a cyanobacterial metallochaperone: Insight into an atypical copper-binding motif, *J. Biol. Chem. 279*, 27502−27510.
25. Borrelly, G. P., Blindauer, C. A., Schmid, R., Butler, C. S., Cooper, C. E., Harvey, I., Sadler, P. J., and Robinson, N. J. (2004) A novel copper site in a cyanobacterial metallochaperone, *Biochem. J. 378*, 293−297.
26. Busenlehner, L. S., Pennella, M. A., and Giedroc, D. P. (2003) The SmtB/ArsR family of metalloregulatory transcriptional repressors: Structural insights into prokaryotic metal resistance, *FEMS Microbiol. Rev. 27*, 131−143.
27. Liu, T., Golden, J. W., and Giedroc, D. P. (2005) A zinc(II)/lead(II)/cadmium(II)-inducible operon from the cyanobacterium *Anabaena* is regulated by AztR, an α3N ArsR/SmtB metalloregulator, *Biochemistry 44*, 8673−8683.
28. Rensing, C., Mitra, B., and Rosen, B. P. (1997) The zntA gene of *Escherichia coli* encodes a Zn(II)-translocating P-type ATPase, *Proc. Natl. Acad. Sci. U.S.A. 94*, 14326−14331.
29. Rensing, C., Sun, Y., Mitra, B., and Rosen, B. P. (1998) Pb(II)-translocating P-type ATPases, *J. Biol. Chem. 273*, 32614−32617.
30. Grass, G., Fan, B., Rosen, B. P., Franke, S., Nies, D. H., and Rensing, C. (2001) ZitB (YbgR), a member of the cation diffusion facilitator family, is an additional zinc transporter in *Escherichia coli*, *J. Bacteriol. 183*, 4664−4667.
31. Pennella, M. A., Arunkumar, A. I., and Giedroc, D. P. (2006) Individual metal ligands play distinct functional roles in the zinc sensor *Staphylococcus aureus* CzrA, *J. Mol. Biol. 356*, 1124−1136.
32. VanZile, M. L., Cosper, N. J., Scott, R. A., and Giedroc, D. P. (2000) The zinc metalloregulatory protein *Synechococcus* PCC7942 SmtB binds a single zinc ion per monomer with high affinity in a tetrahedral coordination geometry, *Biochemistry 39*, 11818−11829.
33. Kuzmic, P. (1996) Program DYNAFIT for the analysis of enzyme kinetic data: Application to HIV proteinase, *Anal. Biochem. 237*, 260−273.
34. VanZile, M. L., Chen, X., and Giedroc, D. P. (2002) Structural characterization of distinct α3N and α5 metal sites in the cyanobacterial zinc sensor SmtB, *Biochemistry 41*, 9765−9775.
35. Walkup, G. K., and Imperiali, B. (1997) Fluorescent chemosensors fr divalent zinc based on zinc finger domains. Enhanced oxidative stability, metal binding affinity, and structural and functional characterization, *J. Am. Chem. Soc. 119*, 3443−3450.
36. Berjanskii, M. V., Neal, S., and Wishart, D. S. (2006) PREDITOR: A web server for predicting protein torsion angle restraints, *Nucleic Acids Res. 34*, W63−W69.
37. Banci, L., Bertini, I., Del Conte, R., Markey, J., and Ruiz-Duenas, F. J. (2001) Copper trafficking: the solution structure of *Bacillus subtilis* CopZ, *Biochemistry 40*, 15660−15668.
38. De Marac, N. T., and Houmard, J. (1987) *The Cyanobacteria*, Elsevier Science Publishing Co., Inc., New York.
39. Tong, L., Nakashima, S., Shibasaka, M., Katsuhara, M., and Kasamo, K. (2002) A novel histidine-rich CPx-ATPase from the filamentous cyanobacterium *Oscillatoria brevis* related to multiple-heavy-metal cotolerance, *J. Bacteriol. 184*, 5027−5035.
40. Pountney, D. L., Tiwari, R. P., and Egan, J. B. (1997) Metal- and DNA-binding properties and mutational analysis of the transcription activating factor, B, of coliphage 186: A prokaryotic C4 zinc-finger protein, *Protein Sci. 6*, 892−902.
41. Busenlehner, L. S., Weng, T. C., Penner-Hahn, J. E., and Giedroc, D. P. (2002) Elucidation of primary (α(3)N) and vestigial (α(5)) heavy metal-binding sites in *Staphylococcus aureus* pI258 CadC: Evolutionary implications for metal ion selectivity of ArsR/SmtB metal sensor proteins, *J. Mol. Biol. 319*, 685−701.
42. Busenlehner, L. S., Cosper, N. J., Scott, R. A., Rosen, B. P., Wong, M. D., and Giedroc, D. P. (2001) Spectroscopic properties of the metalloregulatory Cd(II) and Pb(II) sites of *S. aureus* pI258 CadC, *Biochemistry 40*, 4426−4436.
43. Payne, J. C., ter Horst, M. A., and Godwin, H. A. (1999) Lead Fingers: Pb^{2+} Binding to Structural Zinc-Binding Domains Determined Directly by Monitoring Lead-Thiolate Charge-Transfer Bands, *J. Am. Chem. Soc. 121*, 6850−6855.
44. Magyar, J. S., Weng, T. C., Stern, C. M., Dye, D. F., Rous, B. W., Payne, J. C., Bridgewater, B. M., Mijovilovich, A., Parkin, G., Zaleski, J. M., Penner-Hahn, J. E., and Godwin, H. A. (2005) Reexamination of lead(II) coordination preferences in sulfur-rich sites: Implications for a critical mechanism of lead poisoning, *J. Am. Chem. Soc. 127*, 9495−9505.
45. Banci, L., Bertini, I., Ciofi-Baffoni, S., Gonnelli, L., and Su, X. C. (2003) A core mutation affecting the folding properties of a soluble domain of the ATPase protein CopA from *Bacillus subtilis*, *J. Mol. Biol. 331*, 473−484.
46. Okkeri, J., and Haltia, T. (2006) The metal-binding sites of the zinc-transporting P-type ATPase of *Escherichia coli*. Lys(693) and Asp(714) in the seventh and eighth transmembrane segments of ZntA contribute to the coupling of metal binding and ATPase activity, *Biochim. Biophys. Acta 1757*, 1485−1495.
47. Dutta, S. J., Liu, J., and Mitra, B. (2005) Kinetic analysis of metal binding to the amino-terminal domain of ZntA by monitoring metal-thiolate charge-transfer complexes, *Biochemistry 44*, 14268−14274.
48. Mitra, B., and Sharma, R. (2001) The cysteine-rich amino-terminal domain of ZntA, a Pb(II)/Zn(II)/Cd(II)-translocating ATPase from *Escherichia coli*, is not essential for its function, *Biochemistry 40*, 7694−7699.
49. Liu, J., Dutta, S. J., Stemmler, A. J., and Mitra, B. (2006) Metal-binding affinity of the transmembrane site in ZntA: Implications for metal selectivity, *Biochemistry 45*, 763−772.
50. Bunce, J., Achila, D., Hetrick, E., Lesley, L., and Huffman, D. L. (2006) Copper transfer studies between the N-terminal copper binding domains one and four of human Wilson protein, *Biochim. Biophys. Acta 1760*, 907−912.
51. Banci, L., Bertini, I., Ciofi-Baffoni, S., Chasapis, C. T., Hadjiliadis, N., and Rosato, A. (2005) An NMR study of the interaction between the human copper(I) chaperone and the second and fifth metal-binding domains of the Menkes protein, *FEBS J. 272*, 865−871.
52. Wernimont, A. K., Huffman, D. L., Lamb, A. L., O'Halloran, T. V., and Rosenzweig, A. C. (2000) Structural basis for copper transfer by the metallochaperone for the Menkes/Wilson disease proteins, *Nat. Struct. Biol. 7*, 766−771.
53. Thelwell, C., Robinson, N. J., and Turner-Cavet, J. S. (1998) An SmtB-like repressor from *Synechocystis* PCC 6803 regulates a zinc exporter, *Proc. Natl. Acad. Sci. U.S.A. 95*, 10728−10733.
54. Cavet, J. S., Borrelly, G. P., and Robinson, N. J. (2003) Zn, Cu and Co in cyanobacteria: Selective control of metal availability, *FEMS Microbiol. Rev. 27*, 165−181.
55. Banerjee, S., Wei, B., Bhattacharyya-Pakrasi, M., Pakrasi, H. B., and Smith, T. J. (2003) Structural determinants of metal specificity in the zinc transport protein ZnuA from *Synechocystis* 6803, *J. Mol. Biol. 333*, 1061−1069.
56. Waldron, K. J., Tottey, S., Yanagisawa, S., Dennison, C., and Robinson, N. J. (2007) A periplasmic iron binding protein contributes towards inward copper supply, *J. Biol. Chem. 282*, 3837−3846.
57. Liu, T., Nakashima, S., Hirose, K., Uemura, Y., Shibasaka, M., Katsuhara, M., and Kasamo, K. (2003) A metallothionein and

CPx-ATPase handle heavy-metal tolerance in the filamentous cyanobacterium *Oscillatoria brevis*, *FEBS Lett. 542*, 159−163.
58. Huckle, J. W., Morby, A. P., Turner, J. S., and Robinson, N. J. (1993) Isolation of a prokaryotic metallothionein locus and analysis of transcriptional control by trace metal ions, *Mol. Microbiol. 7*, 177−187.
59. Blindauer, C. A., Harrison, M. D., Robinson, A. K., Parkinson, J. A., Bowness, P. W., Sadler, P. J., and Robinson, N. J. (2002) Multiple bacteria encode metallothioneins and SmtA-like zinc fingers, *Mol. Microbiol. 45*, 1421−1432.
60. Blindauer, C. A., Harrison, M. D., Parkinson, J. A., Robinson, A. K., Cavet, J. S., Robinson, N. J., and Sadler, P. J. (2001) A metallothionein containing a zinc finger within a four-metal cluster protects a bacterium from zinc toxicity, *Proc. Natl. Acad. Sci. U.S.A. 98*, 9593−9598.
61. Grossoehme, N. E., Akilesh, S., Guerinot, M. L., and Wilcox, D. E. (2006) Metal-binding thermodynamics of the histidine-rich sequence from the metal-transport protein IRT1 of *Arabidopsis thaliana*, *Inorg. Chem. 45*, 8500−8508.

BI7006367